AIAA JOURNAL
Vol. 44, No. 12, December 2006

# Experimental and Numerical Study of Cyclogiro Aerodynamics

Gil Iosilevskii* and Yuval Levy†
*Technion—Israel Institute of Technology, 32000 Haifa, Israel*

DOI: 10.2514/1.8227

**A combined experimental and numerical study of a cyclogiro rotor operating at Reynolds numbers about 40,000 has been conducted. The study reveals complex flow field with complex (unsteady) interactions between the blades and the wakes of other blades. In spite of this complexity, time-averaged integral forces acting on the rotor can be predicted by a simple momentum theory, properly corrected for thrust-producing area of the rotor and for large Magnus effect. The effective thrust producing area was estimated to be about half of its projected area, suggesting that the effectiveness of a cyclogiro rotor may be comparable with that of a heavy-loaded helicopter rotor.**

## I. Introduction

THE term "cyclogiro rotor" is commonly used to imply a rotor consisting of a pair of coaxial disks and a number of feathered blades spanning the space between them (Figs. 1–3) [1]. As the disks rotate, the blades' angles of attack (AOA) undulate periodically over one revolution. AOA undulations are induced, through push–pull rods, by an eccentric axis. By changing the position of the eccentric axis relative to the rotation axis, the cyclogiro rotor can be tuned to produce thrust in any direction in the plane of rotation (Fig. 2).

The invention of the cyclogiro rotor can be traced to as early as the end of the 19th century [2], with several patents following during the first few decades of the 20th century. The designs suggested replacing conventional horizontal surfaces by comparably sized cyclogiro rotors, with a resulting vehicle having, at least in theory, both hover and forward flight capabilities. All designs have failed, apparently because of inadequate performance of cyclogiro rotors [3].

The ease with which the direction of thrust of the cyclogiro rotor can be controlled brought a renewed attention to the concept. For example, a recent design [4] suggested installing a few cyclogiro rotors on an airship, where performance is less of an issue and can be sacrificed for improved maneuverability. If cyclogiro rotor effectiveness could be improved, it could also become a viable concept for a hover-capable micro-UAV. For example, four cyclogiro rotors in a cross configuration result in a hovering vehicle that is capable of translating in all directions without changing its angular orientation (Fig. 3).

Because we are unaware of any closed-form analytical theory of a cyclogiro rotor that may adequately explain the reasons for its ineffectiveness, we have undertaken a combined numerical and experimental study, with particular emphasis on small-scale, low Reynolds number, applications. To this end we have designed and constructed a small, about 4 in. across, electrically driven rotor (Fig. 1); fitted it on a sting balance, and measured its time-averaged performance at various configurations and various operating conditions. This experimental data comprised the basis for the analysis presented herein; the analysis was rationalized using dimensional analysis, analytical blade-element theory of [1], and numerical simulations.

Received 11 February 2004; accepted for publication 22 July 2006. 

*Senior Lecturer, Faculty of Aerospace Engineering. Member AIAA.
†Senior Lecturer, Faculty of Aerospace Engineering. Senior Member AIAA.

The main use of numerical simulations in this study was to provide details of the flow field, which could not be obtained with the present (nontransparent) experimental setup. This end use, which is rather qualitative, allowed some simplification in modeling the rotor for the simulations. In particular, assuming that within a large part of the rotor volume the flow is essentially two dimensional, we replaced the end plates by doubling the span. With simulations yielding essentially the same integral forces as those measured experimentally, we feel confident that this assumption was justified.

## II. Experimental Setup

The experimental model is shown in Fig. 1. It consisted of a single rotor directly driven by a dc motor. The motor was equipped with a speed controller, aimed at keeping the angular velocity $\Omega$ constant under varying load; the angular velocity could be preset at any value between 60 and 630 rad/sec. The rotor could be fitted with either two or four identical blades, each having rectangular planform with chord $c = 22$ mm, span $s = 110$ mm, and NACA0015 cross section. The blades were feathered about their center-of-gravity, 9.9 mm (45% chord) from leading edge, and evenly distributed on an imaginary cylinder of radius $R = 55.8$ mm. Push–pull rods connected the leading edges of the blades (actually, the points located at the distance $h = 9.2$ mm forward of the respective feathering axes) with the eccentric axis. The length of the rods was $l = \sqrt{R^2 + h^2}$, 56.5 mm (Fig. 2).

The eccentric axis could be moved relative to the rotation axis (Fig. 2) by computer-controlled dual-servo actuator (Fig. 1); the distance $e$ between the axes varied between 0 and 5.5 mm, yielding 0 to 40 deg AOA modulation. In a typical experiment, the eccentric axis was moved for about 40 to 60 s in a sinusoidal manner with a period of 10 to 20 s between minimal, 0, and maximal, 5.5 mm, deflection.

The rotor was assembled on a standard 5-component (3 moments and 2 lateral forces) sting balance with its axis collinear with the axis of rotation. Force resolution of the balance was about 0.002 N, moment resolution was 0.0002 Nm. The rotor speed was picked up by an optical sensor counting two lines per revolution. The eccentric axis position, rotor speed, forces, and moments were each sampled at 1 KHz and time averaged over 0.1 s intervals, yielding 400 to 600 test points for each experiment. Air temperature and atmospheric pressure, from which the density $\rho$ was computed, were time averaged over the entire 40 to 60 s of the experiment.

Power required to rotate the rotor was computed from the product of the aerodynamic moment and the angular velocity. Aerodynamic moment was computed by subtracting the product of the angular acceleration of the rotor (which could not be entirely avoided due to the lack of motor power) and the rotor inertia from the measured axial moment.

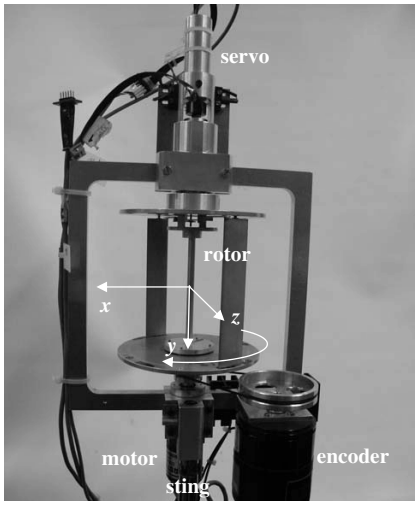


**Fig. 1 The two-bladed version of the rotor used during the experiments.**

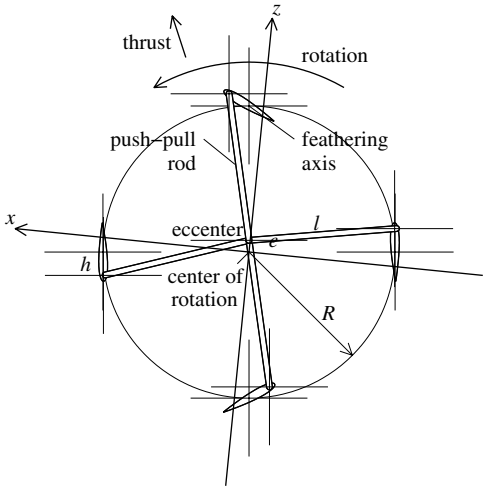


**Fig. 2 Cross section of a four-bladed rotor and the coordinate system.**

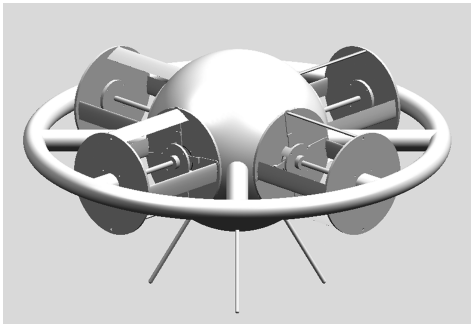

**Fig. 3 A possible cyclogiro configuration for a micro-UAV.**

## III. Numerical Setup

In the numerical simulation, the end plates were omitted to simplify the problem. The chord and radius have been selected so as to replicate the experimental setup; the span has been doubled to reduce the end effects. All simulations have been conducted using the EZNSS flow solver [5–7] at the reference Mach number of 0.12 and Reynolds number of 40,000, roughly corresponding to actual test conditions. Both two- and four-bladed configurations have been addressed, the former with 15 and 25 deg AOA modulations; the latter with 0, 15, and 20 deg. The free stream conditions were set to zero velocity and zero pressure gradient.

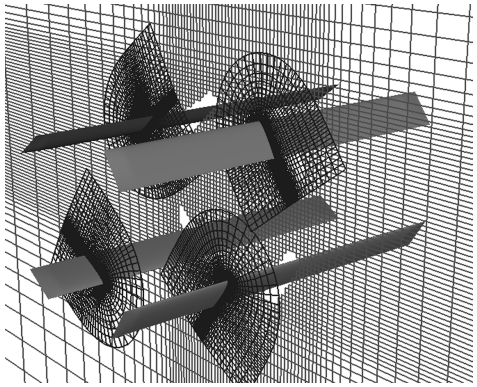

**Fig. 4 Computational mesh.**

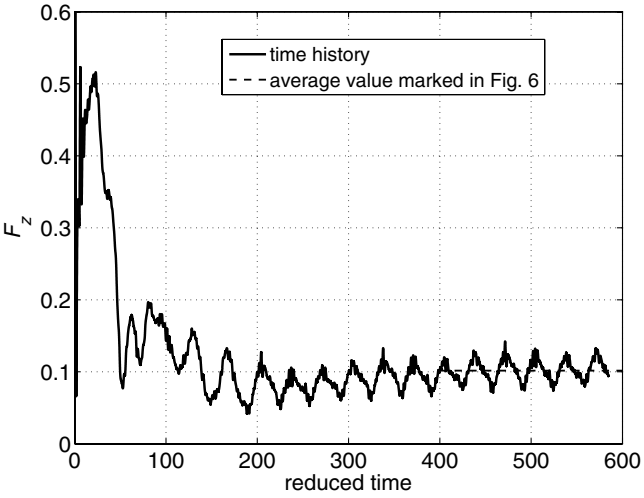


**Fig. 5 Convergence of the $z$ component of the rotor thrust; 4 blades, 15 deg AOA modulation.**

To accommodate the geometry changes that resulted from the motion of the blades, the Chimera [8] scheme has been employed. Body-fixed meshes were generated for each blade ("D"-shaped slices in Fig. 4) and embedded in the global zone. The global mesh was extended to the distance where the interference caused by the rotor died away.

The governing equations solved were the full Navier–Stokes equations assuming laminar compressible flow. Time integration was conducted using the implicit algorithm of Beam and Warming [9,10]. Further details of the computational scheme may be found in [5–7].

All solutions were initiated from the flow at rest, and continued for about 6 to 10 revolutions, depending on the case. After 2 to 3 revolutions the flow invariably reached a fixed-pattern periodic behavior, attributed to the vortex shedding from the blades' surfaces. Figure 5 shows a typical plot demonstrating convergence of the forces.

## IV. Results and Analysis

### A. Definitions

To facilitate the comparison with [1], we shall adopt the same right-handed Cartesian coordinate system, with its $y$ axis coinciding with the axis of rotation and $z$ axis connecting the axis of rotation with the feathering axis when a blade reaches its maximum AOA. This system is shown in Fig. 2.

Concurrently, we shall use $\Omega R$, $\Omega R^2$, $\rho s R(\Omega R)^2$, $\rho s R^2(\Omega R)^2$, and $\rho s R(\Omega R)^3$ as convenient units of velocity, circulation, force, moment (torque), and power, respectively. These units will be implicitly implied hereafter in all figures and formulas. They differ

from standard units used in helicopter theories in having the reference area half (rather than all) of the rotor projected area.

Angular-velocity-based units of velocity and power are applicable regardless of whether the rotor produces thrust or not; in fact, this was one of the reasons why they have been selected this way. However, given nonzero thrust, additional quantities having dimensions of velocity and power can be formed. Indeed, a quantity having the dimension of velocity can be obtained from the square root of the ratio of the thrust to the fluid density and to something having dimensions of area. Concurrently, a quantity having a dimension of power can be obtained from the product of this velocity and the thrust. Because both quantities vanish with the thrust, they are closely associated with the notions of "induced velocity" $v_i$ and "induced power" $P_i$, respectively. Thus, in the present notation,

$$v_i = \sqrt{F/(4k_v)} \tag{1}$$

$$P_i = Fv_i = \sqrt{F^3/(4k_v)} \tag{2}$$

where $F$ is the (reduced) thrust, and $k_v$ is a certain proportionality constant. The odd way it has been introduced in these formulas has its roots in momentum theories [11,12]; it is suggestive of the ratio between the effective thrust-producing area of the rotor and its projection $2Rs$. Noting that both $F$ and $P_i$ have been defined using only half the projected area as the reference area, $k_v$-equals-unity variants of Eqs. (1) and (2) will be found to be identical with Eqs. (2.13) and (2.20) of [12].

### B. Results

Selected results for the time-averaged force and power at 4000 to 6000 rpm (corresponding to chord-based Reynolds numbers of about 34,000 to 50,000) are presented in Figs. 6–8. They will be discussed in the following section. The most conspicuous is, perhaps, the direction of thrust relative to the $z$ axis (Fig. 7): the thrust lags behind the AOA, with the lag angle decreasing as the thrust of the rotor increases. Rotor "stall" is apparent at angles of attack in excess of 26 deg for the two-bladed and 32 deg for the four-bladed configurations; it is marked by dotted lines on all figures.

Noteworthy is the accuracy of the numerical computations. In spite of the complexity of the problem, and in spite of replacing the end plates by doubling the span, the total force estimation error is less than 5%. The direction of thrust leads by about 10 deg, but captures the correct trend. The torque estimation error is less than 20% for all AOA modulations. The accuracy of the numerically computed integral forces gives confidence in the numerically generated flow field; the latter will be used in the following sections to supplement the analysis.

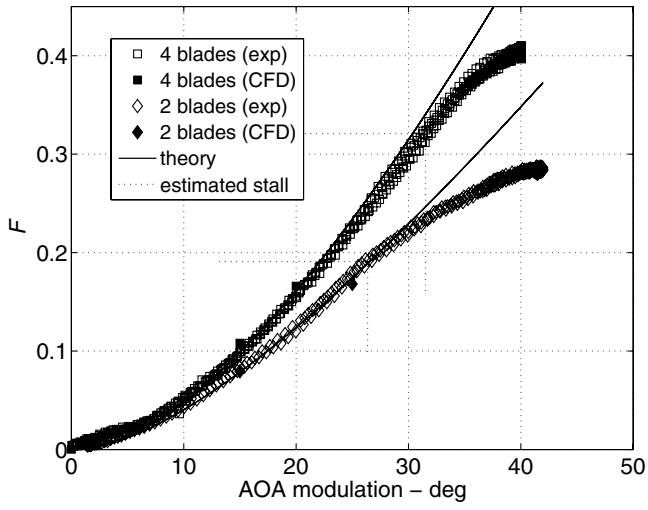


**Fig. 6 Reduced thrust of 2 and 4 bladed rotors.**

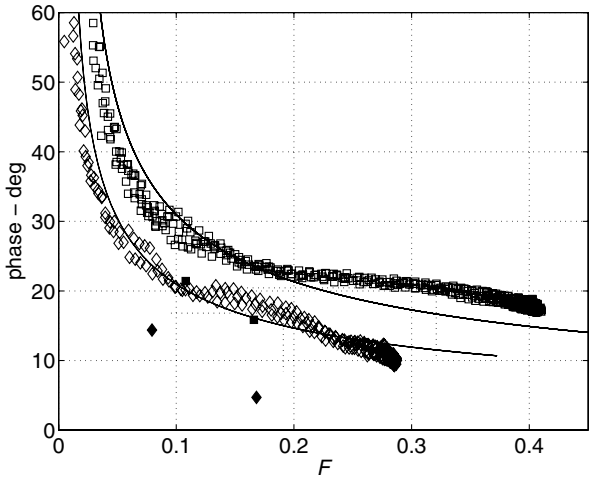


**Fig. 7 The angle between the direction of thrust and the position of the maximum AOA. Notation is as in Fig. 6.**

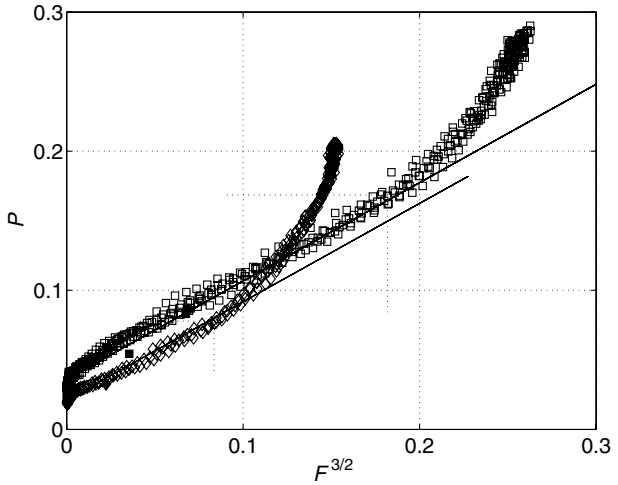


**Fig. 8 Reduced power required to rotate the rotor. Notation is as in Fig. 6.**

### C. Induced Power

Following the simple dimensional analysis presented above, the power required to rotate the rotor should be proportional to the rotor thrust to the power of $\frac{3}{2}$; see Eq. (2). Indeed, this relation between the power and the thrust holds up to the onset of stall (Fig. 8). The proportionality constant is approximately 0.7 for both four- and two-bladed configurations; slightly bigger for the former and slightly smaller for the latter. This is 40% more than the value (0.5) of simplified momentum theory based on uniform velocity over the entire projected area of the rotor [11,12]. Hence, the velocity through the rotor cannot be uniform. Noting that the blades have no angle of attack as they cross the $x$ axis, this result is plausible. A picture of the numerically simulated flow field (Fig. 9) confirms this conclusion.

The proportionality constant (0.7) between the power and thrust at the $\frac{3}{2}$ power implies that roughly half ($k_v = 0.7^2$) of the rotor

**Fig. 9 Instantaneous streamlines in the symmetry plane of the rotor for two consecutive rotor positions.**

projected area $2Rs$ produces thrust. With this empirical correction introduced in Eq. (1), a simple blade-element theory of [1], suggesting

$$F = \frac{cb}{4R}(a\alpha_A - av_i - 3C_d v_i) + \ldots \tag{3}$$

recovers the experimental data found in Fig. 6 to a very good accuracy. In this formula, $b$ is the number of blades, $a$ is the lift slope coefficient of the blade's cross section (we took $2\pi$), $\alpha_A$ is the AOA modulation amplitude, $C_d$ is the blade's profile drag coefficient (as long $C_d \ll a$, this term is negligible), and the ellipses stand for the higher order terms with respect to the eccentric axis offset. [Eq. (3) follows Eq. (26) of [1] with $\alpha_0 = 0$, $\varepsilon = \pi/2$, $\mu = 0$, $\lambda = v_i$.]

The estimate of the thrust-producing area of the rotor can be supported, indirectly, by the stall angle of the blades. The stall condition of the rotor (as opposed to that of the blades) was identified by the break in the slope of the rotor thrust with AOA modulation (Fig. 6). Actual AOA of the blades at the rotor stall was obviously smaller; it can be estimated by subtracting the induced AOA modulation (it approximately equals $v_i$) from the geometric (eccenter-induced) AOA modulation. With $v_i$ computed from the rotor thrust using Eq. (1), the effective AOA modulation at stall turns out to be 8.6 deg for both rotors. This value has been marked by a dotted line in Fig. 10. Noting that the measured (static) stall angle of these blades is about 6 deg and also noting that AOA of a blade only instantaneously reaches its maximal value, the estimate for the induced velocity based on $k_v \sim 0.5$ seems plausible.

An equivalent of $k_v$ in helicopter theory [12] is the *induced power coefficient* $k_{\text{ind}}$; it is related to $k_v$ by $k_{\text{ind}} = 1/\sqrt{k_v}$. The value of $k_{\text{ind}}$ can be found in Fig. 2.10 of [12]. It implies that the value of $k_v$ for a helicopter rotor varies between 0.5 and 0.8, increasing with the thrust coefficient of the rotor. Hence, insofar as the power required to produce thrust is concerned, a cyclogiro rotor is comparable with a heavy-loaded (high thrust coefficient) helicopter rotor.

### D. Parasite Power

The power required to rotate the model rotor at zero thrust $P_0$ goes into the work against aerodynamic drag of the blades (together with their push–pull rods), and the work against aerodynamic drag of the end plates and the encoder drive (Fig. 1). The (reduced) power required to rotate a single blade with no AOA modulation (no thrust) is obviously given by

$$P_0^b = \frac{(1/2)\rho cs(\Omega R)^3 C_d}{\rho sR(\Omega R)^3} = \frac{cC_d}{2R} \tag{4}$$

cf. Sec. IV.A for the unit of power. The power required to rotate $b$ blades fitted into a single rotor should be, approximately, $b$ times that much. In contrast, the power required to rotate the end plates and the encoder drive $P_0^e$ should be practically independent of $b$. Thus, fitting $P_0 = P_0^b b + P_0^e$ to the data measured at about the same rotor speeds yielded $P_0^b \approx 0.0079$ and $P_0^e \approx 0.0056$. Hence, $C_d \approx 0.04$, by Eq. (4). We could not find measured drag coefficient of NACA0015 section at Reynolds numbers about 40,000, but known results for E61 profile found in [13] render the present estimate, which also includes the drag of the push–pull rods, plausible. We see no simple way to verify the estimate of $P_0^e$, but this part of the parasite power can probably be significantly reduced by a proper design. Should this be the case, Eq. (4) can be used to estimate the power required at zero thrust.

Noteworthy is the fact that on the verge of rotor stall, even with the present (not optimal) design, $P_0$ constitutes about 25% of the total power required to rotate the rotor; slightly more for a two-bladed rotor, slightly less for a four-bladed one. These figures are comparable with a conventional helicopter rotor [12].

### E. Magnus Force

We believe that a large $x$ component of the rotor thrust measured at low to moderate angles of attack can be explained by the Magnus effect [14]. In fact, the instantaneous streamlines of the numerically simulated flow field (Fig. 9) bend in the negative $x$ direction as they cross the rotor volume. This flow structure infers positive (in the same sense as the rotation) circulation about the entire rotor and positive $x$ component of the rotor thrust. This thrust component should be proportional to the induced velocity; this statement follows momentum conservation considerations. Hence, without a loss of generality, one may set $F_x = \Gamma v_i$, where $\Gamma$ is the effective "circulation" about the rotor.

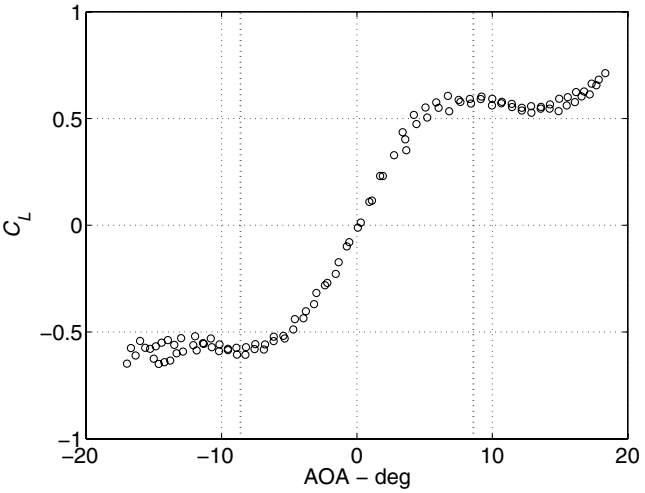


**Fig. 10 Lift coefficient of a single blade (referred to the blade area) at Reynolds number of 41,000.**

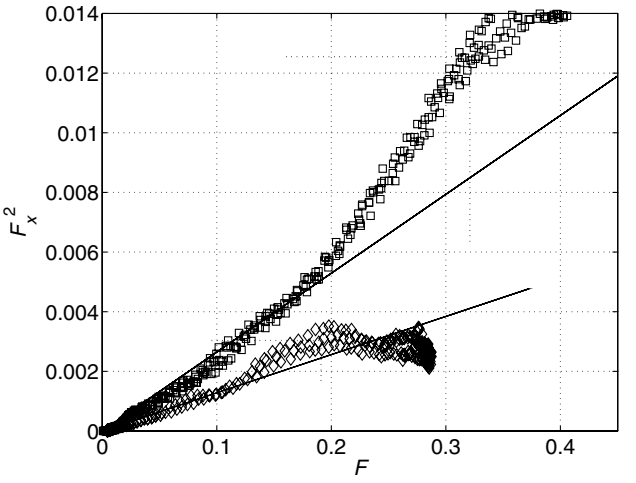


**Fig. 11 *X* component of the reduced force. Notation is as in Fig. 6.**

Noting Eq. (1), this relation implies $F_x^2 = F\Gamma^2/(4k_v)$. Indeed, linear dependence of $F_x^2$ upon $F$ is apparent in Fig. 11 up to about half the stall values of $F$. More careful analysis puts the upper bound of the linear range at AOA modulation of 18 deg for the two-bladed rotor and 24 deg for the four-bladed one. Both correspond roughly to 5 deg effective AOA modulation (geometric modulation less the induced one), and therefore can probably be associated with the onset of the prestall drag rise (Fig. 10).

With $k_v = 0.5$, the slopes marked in Fig. 11 infer $\Gamma \approx 0.16$ for the two-bladed rotor, and $\Gamma \approx 0.23$ for the four-bladed one. Because we obtain no direct proportionality between $\Gamma$ and the number of blades, it must be concluded that the source of the rotor circulation lay not only with the blades, but with other rotating parts as well, in particular, the end plates. This may also explain why numerical simulations, computed without the end plates, have underestimated the $x$ component of the rotor thrust while fitting all other integral parameters.

## V. Conclusions

A combined numerical and experimental study of a cyclogiro rotor operating at Reynolds numbers about 40,000 reveals a complex flow field with complex (unsteady) interactions between the blades and the wakes of other blades. In spite of this complexity, good agreement was found between numerical predictions and experimentally obtained time-averaged integral forces. The numerically simulated flow field was instrumental in interpreting the experimentally measured integral forces.

A large Magnus effect was identified, causing a significant lag (10 to 40 deg) between the direction of thrust and the direction where AOA is maximal. It is plausible that the circulation associated with this effect is caused not only by the blades, but by the end plates as well.

A simple blade-element theory of [1], supplemented by Eq. (1), and empirically corrected for the thrust-producing area of the rotor, predicts the thrust of the rotor with practically adequate accuracy. It was found that the effective thrust-producing area of the cyclogiro rotor is about half of its projected area. In other words, the power required to produce thrust is higher by about 40% than that predicted by the momentum theory based on uniform velocity over the rotor projected area.

The cyclogiro rotor was found to be comparable in performance with a heavy-loaded (high thrust coefficient) helicopter rotor. Accordingly, as far as we can see it, the disadvantage of the cyclogiro rotor lay not in its aerodynamic performance, but in its intrinsic design. The centrifugal forces acting on cyclogiro blades exceed the aerodynamic forces by almost 2 orders of magnitude. It implies either weight penalty for making the blades strong enough, or drag penalty, if struts or wires are added to stiffen the construction. We believe that inadequate performance of the rotor reported in the literature can be attributed mainly to an excessive drag of the blade supporting devices.

## Acknowledgments

The authors would like to thank Daniel Weihs from the Faculty of Aerospace Engineering for bringing the notion of cyclogiro to their attention, Arthur Grunwald for designing and constructing the controllers, and the TAMAM division of IAI for help in manufacturing the experimental model.

## References

[1] Wheatley, J. B., "Simplified Aerodynamic Analysis of the Cyclogiro Rotating Wing System," NACA TN 467, 1933.

[2] Azuma, A., *The Biokinetics of Flying and Swimming*, Springer–Verlag, Berlin, 1992.

[3] Wheatley, J. B., and Windler, R., "Wind-Tunnel Tests of a Cyclogiro Rotor," NACA TN 528, 1935.

[4] Boschma, J. H., "Modern Aviation Applications for Cycloidal Propulsion," AIAA Paper 2001-5267, Oct. 2001.

[5] Levy, Y., "Numerical Simulation of Dynamically Deforming Aircraft Configurations Using Overset Grids," *Journal of Aircraft*, Vol. 38, No. 2, 2001, pp. 349–354.

[6] Moryossef, Y., and Levy, Y., "Effect of Oscillations on Airfoils in Close Proximity to the Ground," *AIAA Journal*, Vol. 42, No. 9, 2004, pp. 1755–1764.

[7] Adar, M., and Levy, Y., "Numerical Simulation of Flare Safe Separation," *Journal of Aircraft*, Vol. 43, No. 4, 2006, pp. 1129–1137.

[8] Benek, J. A., Buning, P. G., and Steger, J. L., "A 3-D Chimera Grid Embedding Technique," AIAA Paper 85-1523, July 1985.

[9] Beam, R. M., and Warming, R. F., "An Implicit Fininite-Difference Algorithm for Hyperbolic Systems in Conservation Law Form," *Journal of Computational Physics*, Vol. 22, Sept. 1976, pp. 88–110.

[10] Beam, R. M., and Warming, R. F., "An Implicit Factored Scheme for the Compressible Navier–Stokes Equations," *AIAA Journal*, Vol. 16, No. 4, 1978, pp. 393–402.

[11] Von Mises, R., *Theory of Flight*, McGraw–Hill, New York, 1945, pp. 285–350.

[12] Stepniewski, W. Z., and Keys, C. N., *Rotary-Wing Aerodynamics*, Vol. 2, Dover, New York, 1984, p. 30.

[13] Grundy, T. M., Keefe, G. P., and Lowson, M. V., "Effects of Acoustic Disturbances on Low Re Airfoil Flows," in *Fixed and Flapping Wing Aerodynamics for Micro Air Vehicle Applications*, edited by Mueller, T. J., AIAA, Reston, VA, 2001, p. 100.

[14] Batchelor, G. K., *Introduction to Fluid Dynamics*, Cambridge University Press, Cambridge, England, 1990, p. 427.

K. Ghia
*Associate Editor*